Functional self-nonamerization of the Type III translocase chaperone/exported protein receptor

Biao Yuan[1], Athina G. Portaliou[1], Yichen Li[2], Jiri Wald[4,5,6], Jochem H. Smit[1,2], Harveer Singh Dhupar[3], Bindu Y. Srinivasu[1], Maria S. Loos[1], Charalampos G. Kalodimos[7], Franck Duong[3], Thorben Cordes[2,8], Thomas C. Marlovits[4,5,6], Anastassios Economou[1]* and Spyridoula Karamanou[1]*

[1] KU Leuven, Department of Microbiology and Immunology, Rega Institute for Medical Research, Laboratory of Molecular Bacteriology, B-3000 Leuven, Belgium

[2] Molecular Microscopy Research Group, Zernike Institute for Advanced Materials, University of Groningen, Nijenborgh 4, 9747 AG Groningen, The Netherlands

[3] Department of Biochemistry and Molecular Biology, Faculty of Medicine, Life Sciences Institute, University of British Columbia, Vancouver, Canada

[4] Centre for Structural Systems Biology (CSSB), Notkestrasse 85, D-22607 Hamburg, Germany

[5] University Medical Center Hamburg-Eppendorf (UKE), Institute for Structural and Systems Biology, Notkestrasse 85, D-22607 Hamburg, Germany

[6] German Electron Synchrotron Centre (DESY), Notkestrasse 85, D-22607 Hamburg, Germany

[7] Department of Structural Biology, St. Jude Children's Research Hospital, 263 Danny Thomas Place, Memphis, Tennessee 38105

[8] Physical and Synthetic Biology, Faculty of Biology, Ludwig Maximilians-Universität München, Großhadernerstr. 2-4, 82152 Planegg-Martinsried, Germany

*For correspondence:

Spyridoula Karamanou (lily.karamanou@kuleuven.be)

Anastassios Economou (tassos.economou@kuleuven.be)

Character count incl. spaces: 44,236

Keywords: EPEC/ *in vitro* reconstitution/ export apparatus/ translocase/ Type III secretion

Abstract

The Type III protein secretion (T3S) pathway is widespread in bacterial Gram-negative pathogens. It comprises the injectisome with a cytoplasm-facing inner membrane translocase and a surface-exposed needle. The translocase comprises a conical $SctR_5S_4T_1$ export channel, decorated by SctU, and enveloped by SctV. The large cytoplasmic domain (C-domain) of SctV binds T3S chaperone/exported protein and forms a putative ante-chamber leading to the membrane translocase. Here we probed the mechanism of assembly and function of SctV. Using live cell imaging, SctV was shown to assemble in peripheral oligomeric clusters in both EPEC and a non-T3SS harbouring *E.coli* strain. Non-ionic detergents extracted SctV homo-nonamers from membranes of both strains. His-$SctV_9$ reconstituted in peptidiscs revealed an elongated, tripartite particle of ~22nm with a membrane domain and a narrower linker connecting to a C-domain. The C-domain assembles in a hollow asymmetric ring with a 5-6 nm-wide inner opening. $SctV_9$ is necessary and sufficient to act as a receptor for two different chaperone/exported protein pairs by binding them at distinct C-domain sites identified by immobilized peptide arrays. Binding sites are not only important for binding but also essential for secretion suggesting a close mechanistic link between the receptor and secretion activities. These findings advance structural understanding of injectisome assembly and reveal that chaperone/exported protein targeting is mechanistically uncoupled from the succeeding translocation step.

Word count: 213

Author summary

The export apparatus of the Type III secretion pathway is conserved in flagellar and virulence injectisomes. Its major component SctV, is essential for T3S substrate targeting and translocation. Here, we analysed SctV assembly and function as a receptor for targeting T3S exported proteins. SctV was shown to self-nonamerize, in a structure that is sufficient for functional binding of chaperone/exported protein complexes. Nonameric SctV reconstituted in peptidiscs and its nonameric ring-forming cytoplasmic domain reveal structural features and lay the foundation for high-resolution cryoEM. These tools set the stage for mechanistic dissection of the structural interactions of the export apparatus with the exported proteins, independently of the transmembrane crossing reaction.

INTRODUCTION

The type III protein secretion system (T3SS) is widely used by many Gram-negative pathogenic or symbiotic bacteria to inject proteins directly into eukaryotic host cytoplasms (1, 2). T3SS comprises the "injectisome", a nano-syringe bridging the bacterial and eukaryotic cytoplasms. Injectisomes comprise four parts (Fig. 1A): a) a ~32-36nm-long trans-envelope "basal body" composed of stacked rings b) an inner membrane-embedded "export apparatus", located at the basal body base c) a circular cytoplasmic sorting platform, including the ATPase complex, that protrudes ~28nm intro the cytoplasm and has a diameter of ~32nm d) a filamentous needle lying at the top of the injectisome, that protrudes from within the basal body to the extracellular milieu, and carries a "translocon" at its tip (1-5). Translocons form pores in the host plasma membrane through which effectors are delivered (6).

The unifying nomenclature Sct (Secretion and cellular translocation) is used for the conserved components of the pathogenic/symbiotic injectisomes across bacteria (7, 8)(www.stepdb.eu). Species/genus suffixes in subscript are added here to denote Sct components from other bacteria (e.g. $_{Sf}$Sct for *Shigella flexneri*).

The export apparatus is thought to be the translocase that mediates chaperone/exported protein targeting, substrate switching from one class to another, and substrate translocation (2, 9). Five components (SctRSTU and V) of the export apparatus contain large hydrophobic transmembrane domains, which challenge structural characterization and functional definition of the apparatus. This is further frustrated by the peripheral nature of the association of SctRST with SctV seen from cryo-ET analysis (3, 4). SctV and U also contain large C-terminal cytoplasmic domains. SctV is a nonamer that forms with its C-domain a large cytoplasmic ring with a ~5nm vestibule connected to the N-terminal membrane part with narrow stalks (10)(Fig. 1A). The isolated cytoplasmic domain of *Shigella flexneri* $_{Sf}$SctV-C crystalized as a ring structure with an external diameter of 11-17nm and a

height from the membrane surface of ~5.5 nm (3, 10). Similarly, the flagellar SctV(FlhA)-C forms rings with an external diameter of 10.1 ± 0.6 nm and a height of 5.1 ± 0.4 nm (11-13). The ATPase is seen in cryo-ET images at a significant distance from SctV (~5 nm; (3, 4) and may connect with the SctV cytoplasmic ring indirectly, perhaps through the elongated SctO stalk (14-17). Additional peripheral bridges formed by the other components of the cytoplasmic sorting platform keep it in place juxtaposed to SctV even when the stalk is missing (4). Whether the ATPase/stalk/SctV C-domain display quaternary dynamics during the translocation cycle is unknown.

The monomeric cytoplasmic domains of SctVs (SctV-C) expressed as individual polypeptides interact with chaperone/exported protein complexes in solution (12, 18, 19) with a dissociation constant (K_d) of ~20 μM (19). Chaperone/exported protein complexes also interact with the hexameric ATPase of the system in NMR-identified complexes (20) and with cytoplasmic platform components in pull-down experiments (17, 21, 22). Although the order of chaperone/exported protein interactions with machinery components during secretion remains debatable, such interactions presumably attract exported substrates to SctV (9, 19), dissociate them from chaperones, let them diffuse to the SctV vestibule and, finally, to the inner membrane SctV/RSTU channel for export, possibly via a putative channel running longitudinally through SctRST (23, 24). Although the internal SctRST pathway is closed in all available structures (24, 25), it may dilate like a diaphragm. These steps are poorly understood, have not been reconstituted *in vitro,* and the precise order and roles of the translocase components are unknown.

cryo-ET revealed that within the assembled injectisome, $_{Se}$SctRST of *Salmonella enterica* sits on top of SctV in an inverted cone formation that is largely peirplasmically exposed and only partially buried in the inner membrane plane (3, 25). It is kept in this periplasmically protruding state apparently through contacts with the SctJ lipoprotein and lipids (25). A similar arrangement was seen in the flagellar T3S (23). The intricate formation

of the injectisome rings would imply possible architectural dependence of one sub-structure on the other and perhaps suggest a temporal order of addition of each element because of these associations. Nevertheless, deletion of *sctV* does not prevent correct injectisome assembly including that of the cytoplasmic sorting platform, the SctRST inverted cone, that should be internal to SctV ring, and the SctD that surrounds SctV externally (3, 4). These data suggest that assembly of SctV may retain a significant autonomy from that of the other architectural components.

Using the Gram-negative pathogen enteropathogenic *Escherichia coli* (EPEC), a serious diarrhea threat to children in developing countries (26), we recently reconstituted T3SS substrate membrane targeting process *in vitro* using inverted inner membrane vesicles (IMVs) harbouring EPEC injectisomes. We revealed a novel mechanism that governs both protein export membrane targeting and switching from translocator (middle substrate) to effector (late substrate) export (9). We now focus on the assembly and receptor function of the translocase machinery. We report that nonamers of $_{EPEC}$SctV and of its C-domain self-assemble *in vivo* in the absence of any other T3S components. Purified His-SctV$_9$ was reconstituted in peptidiscs and analyzed by negative staining electron microscopy. Peptidisc-reconstituted SctV$_9$ is a particle with a hydrodynamic diameter of ~22 nm with distinct membrane-inserted and cytoplasmic moieties connected by a narrower stalk. Its C-domain assembles into nonameric rings with an internal pore of a 5-6 nm diameter. SctV$_9$ is necessary and sufficient to act as a functional receptor for chaperone/exported protein complexes in the absence of ongoing secretion and/or other injectisome components. Specific patches on SctV C-domain are essential for chaperone/ exported protein complexes to bind as demonstrated using immobilized peptide arrays and confirmed with mutational analysis that resulted in abrogation of secretion. Our findings uncouple the targeting of chaperone/exported protein from the succeeding translocation step and provide further

structural understanding of SctV assembly. As such they lay the foundations for future mechanistic and structural dissection of the T3S translocase.

RESULTS

SctV forms multimeric clusters *in vivo*

To analyze SctV membrane assembly *in vivo* we fused eYFP to the N-terminus of SctV. eYFP-SctV was synthesized in EPEC from a tetracycline promoter-driven expression-vector with addition of anhydrotetracycline (AHT; 20 ng/mL) as described for SctV (9). EPEC∆*sctV,* a non-polar deletion strain, is similarly complemented *in vivo* by *sctV* (Fig. S1A, lane 3) and *eyfp-sctV* (lanes 5-6). eYFP-SctV assembles in distinct focal points or clusters in the periphery of EPEC∆*sctV* cells (Fig. 1B) seen by live-cell fluorescence microscopy.

To test if SctV assembly in clusters *in vivo* requires any other T3S components or if it self-assembles, we imaged the *E.coli* lab strain C41, that is devoid of an injectisome, carrying *eyfp-sctV*. C41/*eyfp-sctV* cells synthesized a similar amount of eYFP-SctV as EPEC∆*sctV/eyfp-sctV* at 20 ng/mL AHT (Fig. S2A; 20 ng/mL used hereafter) that became visible after ~20 min (Fig. 1C; Fig. S2B). This presumably also encompasses the maturation time for the fluorophore (27). As in EPEC∆*sctV* (Fig. 1B), eYFP-SctV synthesized in C41 also showed a distinct peripheral punctate staining and (Fig. 1C), indicating that the apparent eYFP-SctV clustering *in vivo* is an inherent property of SctV.

The punctate staining pattern of eYFP-SctV was characteristic and distinct from that of other fluorescent fusion protein markers that showed either diffuse staining all over the cytoplasm (eYFP, Fig. 1D) or peripheral staining but of similar intensity (periplasmic TorA (Fig. 1E)(28); outer membrane BamE (Fig. 1F)(R. Ieva, unpublished); monomeric inner membrane LacY-eYFP (29)(Fig. 1G)].

To quantify SctV clusters we excluded potential artefacts such as larger, highly fluorescent particles accumulated at the poles or at the membrane, suggestive of possible inclusion bodies and aggregates (Fig. S2C). Analysis of ~10-14,000 cells revealed that commonly ~1-4 eYFP-SctV foci form per EPEC∆*sctV* cell and C41 (Fig. S3A) which were distributed along the periphery of the cells (Fig. S3B). Focal points may represent single

eYFP-SctV multimers or clusters of multiple eYFP-SctV multimers within 100 nm of each other. Nevertheless, eYFP-SctV foci systematically fluoresced more strongly than the monomeric inner membrane protein LacY-eYFP, suggesting that SctV assembles in higher order quaternary states (see below).

These data suggested that SctV forms multimeric, presumably inner membrane-embedded assemblies *in vivo.*

SctV natively extracted from membranes is nonameric

To study the oligomeric state and assembly of SctV, we isolated EPEC membranes, treated them with various concentrations of the non-ionic detergent dodecyl-maltoside (DDM), separated the resulting complexes by Blue Native-Polyacrylamide Gel Electrophoresis (BN-PAGE) and visualized them by immuno-staining with an antibody against the C-terminal cytoplasmic domain of SctV (Fig. 2A).

DDM concentrations ≤0.7% [w/v; 13.2 mM; ~80-fold above the critical micellar concentration (CMC_{H2O} = 0.17 mM)] did not solubilize discrete SctV-containing complexes (Fig. 2B, lane 2). At DDM concentrations ≥1.0%, the SctV-containing species migrated as a tighter band, with an apparent mass of ~700 kDa, consistent with the mass of a stable nonamer (Fig. 2B, lanes 3-5). Nonameric rings of the C-terminal domain have been crystalized from *Sf*SctV-C (10). Also, nonamers of full length *Se*SctV have been proposed by electron cryotomography analysis of membrane-embedded injectisomes (3, 4).

When membranes were solubilized with 0.8% DDM, higher order SctV-containing complexes with apparent sizes of ~1 MDa immuno-stained with α-SctV-C (Fig. 2B, lane 6, bracket). These might be sub-assemblies of the injectisome [mass >3 MDa; at least 18 different proteins (8, 30)]. When 0.8% DDM extracts were treated with additional DDM to a final concentration of 1.8%, a sharp band of $SctV_9$ was obtained (Fig. 2B, lane 7) indicating that the assembled nonamer was a pre-existing component of the ~1 MDa species.

Elevated amounts of DDM likely dissociated all other partner subunits but left the $SctV_9$ intact.

These data suggested that full length SctV in EPEC membranes assembles in stable, detergent-extractable, nonameric assemblies that easily dissociate from, and, therefore, weakly associate with other injectisome components.

Injectisome-independent self-assembly of SctV nonamers in membranes

SctV proteins might assemble on demand by enveloping existing membrane-embedded cores of SctRSTU or other injectisome components (4, 31-33). However, EPEC-derived $SctV_9$ is stable at up to 1.8% DDM (Fig. 2B) and $SctV_9$ forms clusters *in vivo* in C41 (Fig. 1C) in the absence of any other injectisome components. This raised the possibility that SctV might self-assemble and nonamerize in membranes unaided by other injectisome components.

To test this directly, we over-expressed the *sctV* gene behind a T7 promoter in C41 cells grown in LB medium (Fig. S4A, lanes 1 and 3). The membranes were isolated and membrane-embedded SctV complexes were characterized as above. At low DDM concentrations (0.4% DDM), C41 extracts contained negligible amounts of extracted SctV (Fig. 2C, lane 2), while at DDM concentrations above 0.6%, discrete nonameric species of SctV of ~700 kDa were detected (Fig. 2C, lanes 3-7), similar in size to those seen in the EPEC-derived extracts (Fig. 2B, lanes 3-5). One visible difference though was that $SctV_9$ extraction from C41 membranes initiated at almost half the DDM concentration needed to extract it from EPEC membranes (Fig. 2C). Perhaps, in EPEC, export apparatus components such as RSTU may further stabilize membrane-embedded and assembled $SctV_9$.

The $SctV_9$ species can also be extracted with other non-ionic detergents (Triton X-100, digitonin; Fig. S4B), suggesting a stable, pre-existing, detergent-independent,

oligomeric state. $SctV_9$ in C41 membranes was destabilized and aggregated by heat treatment (Fig. S4C) or once purified from membranes, dissociated into smaller complexes when treated with an ionic detergent (Fig. S4D), but was very stable at high concentrations of non-ionic detergents (Fig. S4E and F).

We concluded that $SctV_9$ can stably self-nonamerize in the absence of any scaffold provided by other T3S components.

$SctV_9$ forms weak complexes with SctRSTU

The available structural information (3, 23), the easier extraction of $SctV_9$ from C41 membranes by DDM (Fig. 2C) and the higher $SctV_9$-containing species seen in EPEC membranes at 0.8% DDM extraction, collectively suggested that $SctV_9$ may directly interact with additional injectisome components. We tested directly whether the export apparatus components SctRSTU form complexes with $SctV_9$. His-SctRSTU synthesized in C41 from a plasmid behind a T7 promoter, give rise to a complex that is best extracted with 3.6% digitonin and has a mass of ˜240kDa when analyzed by BN-PAGE and immuno-stained with α-EscU C-domain antibody (Fig. 2D, lane 1). This apparent mass would be consistent with the R_5:S_4:T_1:U_1 stoichiometry anticipated from cryoEM and MS experiments (3, 23-25). When co-synthesized with SctV, a higher order species is observed (Fig. 2E, lane 4) and once sequentially treated with 1.8% DDM (w/v) the nonameric species of SctV appears as a prominent sharp band, indicating complex dissociation (Fig. 2F, lane 2). Even at the low DDM concentration of 0.8% used, this >1M Da species runs as a diffuse band suggesting poor stability and increased dynamics.

To determine if there is a required order of events in the membrane assembly of SctV and the contribution of SctRSTU, we used C41 carrying two compatible plasmids, one with *escV* behind an Arabinose promoter and another with *his-sctRSTU* behind a T7 promoter that is transcribed in the presence of IPTG. *his-sctRSTU* synthesis was induced first and

was followed by induction of *escV*. While induction of *escV* synthesis alone yields the previously seen SctV nonamer (Fig. 2G, lane 1), when SctV is made in cells with pre-formed His-SctRSTU, higher mass super-complexes are observed (Fig. 2G, lane 2). We could not successfully perform the reverse-order experiment.

Collectively, these data suggested that $SctV_9$ forms detectable but weak associations with SctRSTU that can also be pre-assembled in the membrane prior to $SctV_9$ assembly.

Contributions of the N- and C-terminal domains of SctV in multimerization

SctV comprises a 34.8 kDa N-terminal domain with 8 predicted transmembrane helices connected by a ~3.0 kDa linker to a 37.1 kDa C-terminal cytoplasmic domain (12). To determine which segment is important for nonamerization, His-tagged N-terminal and C-terminal polypeptides (SctV-N and SctV-C; Fig. 3A, top) were synthesized in C41 and their oligomerization properties were compared to those of SctV.

Cytoplasmic and membrane extracts were fractionated by ultra-centrifugation. Full length SctV and SctV-N were mainly distributed in the membrane fraction, while most of SctV-C was detected in the cytosolic fraction (Fig. 3A, lanes 1-3). To exclude co-sedimentation with membranes due to aggregation and inclusion body formation, the membrane fraction was further washed with 8M Urea in two steps. Full length SctV and SctV-N remained largely in the urea-insoluble membrane fraction (Fig. 3A, top and middle, lane 7), while SctV-C was completely urea-extracted (Fig. 3A, bottom, lane 4). These findings suggested that SctV-N is competent at membrane integration in the presence or absence of the C-domain.

To test if membrane-embedded His-SctV-N can inherently oligomerize, we extracted it and analysed it by BN-PAGE (Fig. 3B). His-SctV-N migrates diffusely at apparent masses of 200-500 kDa (lane 2, bracket), that are discrete from $SctV_9$ (lane 1). This might imply formation of dynamic, unstable oligomers.

We next tested if His-SctV-C oligomerizes inherently. For this we characterized His-SctV-C by analytical gel permeation chromatography coupled to multi-angle and quasi-elastic light scattering detectors (GPC-MALS/QELS) that can provide accurate *ab initio* masses and hydrodynamic Stokes radii. His-SctV-C_9 purified by metal affinity chromatography and sucrose gradient ultra-centrifugation (Fig. 4A, Fig. S5A) had a mass of 384.3 (± 3.5) kDa and a diameter of 15.14 (± 0.82) nm by GPC-MALS/QELS (Fig. 4B; Fig. S5B and C) and 379.2 (± 2.07) kDa by native mass spectrometry (Fig. 4C), both in good agreement to the theoretical mass of 374.9 kDa of His-SctV-C_9.

We also analysed His-SctV-C_9 by negative staining electron microscopy. Thousands of particles (Fig. 4D, overview) showing ring structures were identified with modest heterogeneity and distributed into at least 3 classes that were averaged (Fig. 4D, “2D Classes”). His-SctV-C_9 forms ring structures with an outside diameter of 15-18 nm and an inner diameter of 5-6 nm. The ring periphery shows 9 distinct densities presumably corresponding to individual protomers. Unlike the proposed crystal-structure-derived model that shows symmetric arrangement of the nine subunits (10), the subunits in the negatively stained ring structures display detectable asymmetry. It is not currently clear if this reflects the inherent dynamics of the rings or handling heterogeneity.

We concluded that SctV-C has a strong tendency to nonamerize. SctV-N may aid this by also forming weak oligomeric assemblies in the membrane.

Peptidisc-reconstituted His-SctV$_9$ forms tripartite structures containing rings

To determine the ultrastructure of full-length SctV$_9$, we synthesized His-SctV in C41. His-SctV complements the T3S of EPEC∆*sctV* cells (Fig. S1B, lanes 6-8) and forms nonamers like SctV (Fig. S1C, lanes 1 and 2). His-SctV$_9$ was extracted from membranes with 1.8% Triton X-100, and separated from higher order aggregates on a sucrose gradient (Fig. 5A). Fractions enriched in His-SctV$_9$ (as determined by BN-PAGE; Fig. 5B; Fig. S5D)

were collected, pooled and incubated with Ni^{2+}-nitrilotriacetic acid (Ni^{2+}-NTA) resin. Ni^{2+}-NTA resin-bound His-SctV$_9$ assemblies were on-bead reconstituted into peptidiscs using 30% fluorescently labelled peptides [Fig. 5C; (34)]. Peptidisc-reconstituted His-SctV$_9$ (hereafter His-SctV$_9$-PR) migrated on BN-PAGE as a band of ~700-800 kDa, similar to the detergent-extracted species (Fig. 5D). To probe if the peptidisc particles were indeed reconstituted in soluble states in the absence of detergent, we analysed them by clear native PAGE (CN-PAGE), which separates molecules on the basis of charge, mass and shape. Silver-stained CN-PAGE gels of His-SctV$_9$-PR revealed a band of ~700-800 kDa (Fig. 5E) that was also fluorescent, indicating the presence of the bound solubilizing peptides (Fig. 5F).

To characterize His-SctV$_9$-PR at higher resolution and accuracy, we used GPC-MALS/QELS. His-SctV$_9$-PR has a mass of 762.8 ± 6.9 kDa (Fig. 6A, red) consistent with a nonameric species bound to ~17 solubilizing peptides of 4.5 kDa. His-SctV$_9$-PR had a hydrodynamic diameter of 22.0 ± 0.98 nm (Fig. 6A, blue) close to the anticipated dimensions derived from cryo-ET (3).

His-SctV$_9$-PR was next analysed by negative staining transmission electron microscopy. Hundreds of particles (Fig. 6B, overview) showing elongated tripartite (side view) and ring structures (bottom view) were identified. The particles showed significant heterogeneity and could not be class averaged. Nevertheless, side views of individual His-SctV$_9$-PR particles (Fig. 6B) reveal that they comprise three distinct regions likely representing the membrane-embedded and cytoplasmic C-domain parts of SctV connected by a linker as proposed in the models (3, 9, 10) (Fig. 6C).

SctV$_9$ is a necessary and sufficient receptor for chaperone/exported protein complexes

SctV interacts with exported proteins and/or their chaperones and the gatekeeper (9, 19, 35). Acquisition of the nonameric state may be required for high affinity binding. This is

anticipated on the basis of the low affinity of chaperone/exported substrate complexes for a flagellar SctV monomer (19). To determine whether self-assembled $SctV_9$ is functional as an exported protein receptor, we probed its binding to the dimeric chaperone CesT alone or in complex with the effector protein Tir, using an *in vitro* affinity assay developed previously (9). IMVs were prepared from *E. coli* C41, harbouring either *sctV* on a plasmid or the empty vector and were urea-treated to strip away peripheral and non-specifically associated proteins. The external face of the IMVs corresponds to that of the cytoplasm in the cell; their lumen represents the periplasmic face. $SctV_9$-containing, C41-derived IMVs were functionally competent for high affinity saturable binding of CesT or the CesT/Tir complex (Fig. 7A; Fig. S6A), with K_d values equivalent to those measured in IMVs from EPEC cells in the presence of all the complete collection of injectisome components (9). In contrast, IMVs from C41 devoid of SctV showed only a linear, non-specific binding component that did not yield a measurable K_d (Fig. 7A; Fig. S6A). The receptor function of SctV was further corroborated using a second chaperone and chaperone/effector complex CesF/EspF (36) that also bound with high affinity to SctV-containing C41-derived IMVs, but not to C41-derived IMVs not containing SctV (Fig. 7A; Fig. S6B).

Chaperone/exported protein pairs are likely to share common receptor docking regions on the $SctV_9$ receptor (19). Attesting to this, incubation of excess of CesF chaperone (at concentrations of 10-fold K_d) prevents the binding of CesT on IMVs prepared from C41/*sctV* and *vice versa* (Fig. 7A).

Chaperone/exported middle substrate complexes (data not shown) and the SctW gatekeeper (9) bind to six different patches on the SctV C-domain determined using arrays of immobilized peptides. Using the same approach CesT, CesT/Tir, CesF, and CesF/EspF were shown to bind to the same 6 patches plus an additional one (Fig. 7B; Fig. S6C-E). The 7 patches (α–η) may be used in multi-valent binding and come together in 3D space to define 3 wider binding regions (I-III) (Fig. 7C).

Patches α, β and γ (Fig. 7B) are functionally important beyond their *sensu stricto* receptor capacity as demonstrated by site-specific mutagenesis of exclusively surface-exposed residues in these segments (9). Such mutations typically reduce the affinity by up to 10 times but are also required for *in vivo* secretion and infection of Hela cells [(9); Fig. 7D, lane 3, γ shown as an example], even when the K_d is satisfied by large amounts of the ligands (9). Patch ε, is part of the previously uncharacterized region II and its functional importance was probed here by generating a derivative with its surface-exposed residues mutagenized (Fig. S6E). EPECΔ*scV*/*sctV* ε^- is completely defective in *in vivo* secretion and infection of HeLa cells (Fig. 7D, lane 4), and CesT/Tir affinity is compromised (Fig. 7A), indicating that region III is also functionally essential for productive SctV-chaperone interaction and secretion (9).

In agreement to $SctV_9$ being a sufficient membrane receptor for chaperone/exported proteins, in IMVs prepared from C41/*sctV*γ^- cells, SctVγ^- was competent in forming nomamers in the absence of other T3SS components (Fig. S6F) but showed a 3-5-fold affinity reduction for CesT/Tir and CesF/EspF (Fig. 7A).

We concluded that $SctV_9$ embedded in C41 membranes is necessary and sufficient to act as a high affinity receptor for T3S chaperone/exported protein complexes. The important mechanistic implication of this observation is that therefore, the receptor function of SctV neither depends on the presence of any other T3S components nor on ongoing translocation.

DISCUSSION

How injectisomes are assembled first using the Sec system to insert core basal body components and then link these internally with the SctI rod, remains elusive. With the development of *in vitro* reconstitution systems (9, 37) and guidance from cryoEM-derived structures, this issue can now be systematically addressed, and assembly processes can be dissected away from functional ones (i.e. secretory client docking and translocation).

The assembly of the SctRSTU translocase and its large externally enveloping SctV subunit are key to the initiation of the assembly of the filamentous needle complex and the export of downstream components (4, 32). However, the assembly coordination of these components remains poorly understood. The SctRST cone is only partially buried in the membrane plane and plugs peripherally the periplasmic face of SctV (3)(23, 24), or, in its absence, with an invaginating the lipid bilayer (3). The purification of stable SctRSTUV holo-complexes has proven challenging (10, 23), due to disruption of the SctV-RSTU interface by detergents (Fig. 2F). A major mechanistic challenge for the assembly of all these subunits is that although they need to enter the membrane using the universal membrane-protein integration machineries (*e.g.* Sec/SRP, YidC), SctV needs to subsequently multimerize and be “plugged” by SctRSTU. Therefore, it seems unlikely that a closed SctV ring can pre-form first and then diffuse into the membrane until it collides with preformed SctRSTU complexes. In such a case, it would not be possible for SctRSTU to be integrated inside the SctV ring using the Sec machineries. On the other hand, when SctV is deleted, the rest of the injectisome can still assemble and SctRSTU properly acquires its periplasmically-exposed location inside SctD and J (3, 4). Thus, SctV may arrive late to half-pre-assembled injectisomes into which it can integrate to meet an almost periplasmically located SctRST, held in place by a disrupted bilayer (3). In EPEC cells, the plugging of SctV by the SctRSTU cone may be simply a kinetically controlled stochastic event, made possible through tight regulation of transcription and/or translation. This simple scenario would be in agreement

with SctV being synthesized in cells much later than SctRSTU (38). While oligomerization in the presence of other injectisome components *in vivo*, has been implied for $_{YE}$*SctV*-eGFP (33), SctV self-assembles into functional nonamers, driven largely by the SctV C-domain (Fig. 4B-D), *in vivo* and *in vitro* even in cells that have no T3SS injectisome components. This demonstrates that nonamerization is an inherent SctV property.

Our data confirmed and extended previous findings regarding the role of SctV as a chaperone/exported protein receptor in T3SS (9, 19) and revealed SctV to be self-sufficient for this property via its C-domain. T3SS chaperones are structurally distinct and flexible and atomic resolution detail of their binding in the context of the SctV nonamer is missing. Similarly, the path that the exported substrates follow upon their dissociation from their chaperone is unknown. Nevertheless, visualization of the identified generic binding patches on the nonameric model of SctV (Fig. 7C), hints to important functional regions made available in the context of the nonamer. Firstly, a common outward facing cleft on $SctV_9$ might be formed by two adjacent protomers, making use of their regions I and II (Fig. 7C, yellow). Secondly, region III, represented by the essential Patch ε is located inside the pore of the SctV C-domain ring facing the cytoplasm. Several residues in these regions were also identified as important for export chaperone and gatekeeper binding in NMR-solved structures (19) and genetic analyses (14, 15, 39-41) in different SctV homologues (Fig. S6E; green-coloured residues; Table S1). Using different T3SS-chaperones we demonstrated that their binding site on SctV-C is universal and shared (Fig. 7A). The identificatied chaperone binding domains on the SctV-C surface and inside its pore has important mechanistic implications as it demonstrates that while targeting and subsequent secretion are structurally and biochemically separable they must also be somehow connected since the mutated receptor site γ, shows a modest reduction in affinity but completely abrogates secretion.

Future analysis will be necessary to dissect the structural basis of these events. To this end, the low-resolution negatively stained EM structures (Fig. 6) allow us to optimize conditions for future high-resolution cryogenic electron microscopy structures. In addition, our development here of tools like the peptidisc-reconstituted $SctV_9$ pave the way for functional reconstitution of the entire inner membrane translocase in a soluble form. This ushers in biophysical tools to study translocase mechanism and dynamics.

Materials and Methods

For the complete list of strains, plasmids, mutants, primers, buffers, antibodies, see the supplementary material.

Cell growth, induction of gene expression, *in vivo* secretion

EPEC strains were grown in the optimized M9 medium (42) (37°C; 6 h). Plasmid gene expression was induced from the tetracycline promoter (OD_{600}=0.3; AHT; 2.5 ng/mL; 3 h or as indicated). Cells were harvested (5,000 x g; 20 min; 4°C; Sigma 3-16KL; rotor 11180); the spent medium was TCA-precipitated (20% w/v) and resuspended with 50 mM Tris-HCl (pH 8.0) in volumes adjusted according to OD_{600}. An equal number of cells or supernatant volumes derived from an equal number of bacterial cells, were analyzed by SDS-PAGE, and immuno- or Coomasie Blue- stained.

Live-cell imaging

Cells were imaged on inverted fluorescence microscope (Olympus IX-83) with a 1.49 NA oil-immersion objective (Olympus UAPON 100x) and ET442/514/561 Laser triple band set filtercube (69904, Chroma). The excitation light was provided by a 514 nm laser (Sapphire LP, Coherent) and the fluorescence emission was collected on an EM-CCD Camera (Hamamatsu C9100-13). Camera frames were collected using CellSens software (Olympus) for multi-position acquisition.

Brightfield images were flattened by subtracting dark offset and dividing by an empty brightfield image. Fluorescence image were corrected for illumination beam profile and dark count. The brightfield images are segmented to identify cell positions by convolutional neural networks with the U-Net architecture (43-45). Next, individual cells were analyzed with the software ColiCoords (46). Binary objects from segmented images were filtered based on morphological features (size, ellipse axis) to select only single planktonic *E. coli* cells. Next,

the obtained cell objects were further filtered in consecutive steps 1) Shape of the binary image; 2) radius of the cell measured from the brightfield image (C41; 280 nm $\leqslant$ r $\leqslant$ 437 nm, EPEC; 467 nm $\leqslant$ r $\leqslant$ 568 nm); 3) shape of the brightfield image radial distribution; 4) fluorescence intensity, which resulted in removal of out-of-focus cells and overexpressing cells. To localize fluorescent foci, first the cytosolic background was obtained by filtering the images with a spatial median filter (47) (kernel size 5 pixels). Foci were identified in the background-subtracted images by a local maximum filter (48). To remove aggregates and inclusion bodies from the identified peaks, the Zernike moments (49) for each peak were determined (R_2^0), and by thresholding only Gaussian-shaped peaks were selected.

Membrane solubilization and BN-PAGE analysis

Cell pellets were resuspended in Buffer A supplemented with 1 mM $MgCl_2$, 2.5 mM PMSF, and 50 mg/mL DNase and lysed by using French press (1,000 psi; 6 passes). The unbroken cells were removed by centrifugation (3,000 x g; 4°C; 5 min; Sigma 3-16KL; rotor 11180). The membrane fraction was pelleted down by high-speed centrifugation (100,000 x g; 4°C; 30 min; 45Ti rotor; Optima XPN-80, Beckman Coulter). The membrane pellet was resuspended in solubilization buffer, homogenized with a Dounce homogenizer to a final protein concentration of ~40 mg/mL. Membrane proteins were extracted by incubating with non-ionic detergent as indicated (4°C; 1 h). Following ultra-centrifugation (400,000 x g; 4°C; 12 min; rotor TL-100; OptimaMax-XP, Beckman-Coulter), solubilized membrane protein samples (20μl extract with BN-PAGE loading buffer, 10% glycerol) were loaded on 3-12% gradient Bis-Tris NativePAGE™ precast protein gels (Invitrogen) and subjected to BN-PAGE electrophoresis as described previously (50) with little modification. BN-PAGE electrophoresis was performed with anode buffer and cathode buffer 1 using XCell™ *SureLock*™ Mini-Cell (approximately 2.5 hours, 4°C, 100V) until the blue running front has

moved about one-third of gel. Then cathode buffer 1 was replaced with cathode buffer 2 for electrophoresis (15 hours, 4°C, 70V).

'On bead' reconstitution of His-SctV$_9$ in peptidiscs

The 'on-bead' peptidisc reconstitution of His-SctV was conducted as described previously (34) with some modifications. Crude membrane suspensions were derived from C41 cells overexpressing His-*sctV* by French press (6 passes; 1,000 psi; pre-cooled with ice). A total of 10 mL suspension (200 mg/mL) was mixed with 200 μl 100 x protease inhibitor cocktail solution (Sigma Aldrich, Cat. S8830), solubilized in Buffer F (supplemented with 1.8% Triton X-100) and incubated (1 h; 4°C). Insoluble aggregates were removed by centrifugation (20,000 x g, 30 min, 4°C; Sigma 1-16K). Solubilized membrane proteins (1 mL; total of 400 mg) were loaded on a 30 mL 15-35% w/v linear sucrose gradient prepared as previously described (51). Sucrose solutions were made in Buffer G and 25 x 89 mm 38.5 mL open-up polyallomer tubes were used (Beckman Coutler). Ultra-centrifugation was performed (160,000 x g; 16 hours; 4°C; SW 32 Ti rotor; Optima XPN-80, Beckman Coulter) and 1mL fractions were collected and analyzed by BN-PAGE. Fractions containing SctV$_9$ without higher order aggregates of SctV were selected and incubated with 1.5 mL of Ni^{2+}-NTA resin (Qiagen) pre-equilibrated in Buffer F (6 h; 4°C). The Ni^{2+}-NTA beads were transferred to a gravity column, washed with 100 column volumes (CV) of Buffer F supplemented with 0.9% Triton X-100 and 10 CV of Buffer H supplemented with 0.02% Triton X-100, sequentially. Post-washing, 1 CV of Assembly Buffer containing 0.8 mg/mL NSPr mix (1 fluorescent: 2 non-fluorescent NSPr; Peptidisc, an amphipathic bi-helical peptide; PEPTIDISC BIOTECH) in 20 mM Tris-HCl pH 8.0) was added to the beads and incubated (1 h; 4°C). Following washing with buffer H (10 CV), His-SctV$_9$-PR was eluted in 0.5 mL fractions (5 mL of Buffer H + 300 mM imidazole). The elution fractions were loaded onto a Superose™6 10/300 GL column previously equilibrated with buffer L using an ÄKTA Pure system (GE Healthcare).

The purified His-SctV$_9$-PR peptidisc complex was subsequently analyzed by negative-stain electron microscopy.

Purification of His-SctV-C$_9$

C41 cells overexpressing *his-sctV-C* were resuspended in buffer A and lysed by French press 1,000 psi; 5-6 passes; pre-cooled with ice). Insoluble material was removed by centrifugation (100,000 x g; 30 min; 4°C; 45 Ti rotor; Optima XPN-80; Beckman Coulter). The cell lysate supernatant was passed through a Ni^{+2}-NTA resin column (Qiagen), and protein was purified following the manufacturer's instructions. Eluted His-SctV-C was loaded on a 13 mL 15-35% linear sucrose gradient and centrifuged (as described above). Fractions containing mainly His-SctV-C$_9$ were further purified on a Superdex200 10/300 GL column previously equilibrated with buffer M using an ÄKTA Pure system (GE Healthcare). His-SctV-C$_9$ complexes were subsequently analyzed by negative-stain electron microscopy.

Native mass spectrometry

His-SctV-C$_9$ was dialyzed in 50 mM ammonium acetate and analyzed using electrospray ionization mass spectrometer (ESI-MS) with a Q-TOF mass analyzer (Synapt G2 HDMS, Waters) and sodium iodide (2 mg/mL) as a calibrant. The operating parameters for the spectral acquisition were as follows: capillary voltage, 1.8 kV; sample cone voltage, 60 V; extraction cone voltage, 2 V; source temperature, 80°C; desolvation temperature, 150°C; backing pressure, 5.26 mbar; source pressure, 2.08 e^{-3} mbar; Trap, 1.44 e^{-3} mbar. Spectra were acquired in the range of 900−8000 m/z in positive-ion V mode. The molecular mass of the recorded spectra was calculated using MassLynx software (MassLynx version 4.1) by deconvoluting the mass spectra using MaxEnt 1.

Electron microscopy

4 µl samples (50 µg/mL in Buffer M) were applied onto negatively glow-discharged carbon-coated copper grids and negatively stained with freshly prepared 2% uranyl acetate. Grids with full-length $SctV_9$ were imaged with a Talos L120C electron microscope operating at 120 kV at a defocus of ~2 Mm and at a nominal magnification of 91,000 x, resulting at a calibrated pixel size at 1.53 Å on the specimen level. For single-particle analysis of His-SctV-C_9 372 movies were recorded with a Talos Arctica electron microscope operating at 200 kV equipped with a Falcon 3 camera in linear mode with a defocus range of 0.5–1.5 Mm at a calibrated pixel size of 1.22 Å on the specimen using EPU software (FEI Company). Contrast transfer function parameters were determined using CTFFIND4. A total of 122,000 particles were picked using crYOLO 1.3 (52) and extracted from motion corrected movies using RELION3 (53). Extracted particles were subjected to unsupervised 2D classification using ISAC from the SPHIRE software suite (54).

Miscellaneous

In vivo protein secretion, the HeLa infection assay, IMVs preparation, peptide arrays, and determination of equilibrium dissociation constants (K_d) were as described (9)(The details of peptide array and *Kd* determination can be also found in supplementary methods). Ni^{2+}-NTA purification was according to the manufacturer's instructions (Qiagen). Purification of plasmids, PCR, digestion, and DNA fragments were done using Wizard® DNA Clean-Up System from Promega. DNA fragment ligation was done by using T4 DNA ligase as per the manufacturer's protocol (Promega). Sequencing of the genetic constructs was performed by Macrogen Europe. Oligos were synthesized by Eurogentec.

Authors' contributions:

B.Y. performed *in vivo* and *in vitro* assays, molecular cloning, protein purification, GPC-MALS-QELS and reconstituted SctV in peptidiscs; A.G.P. performed membrane binding assays, peptide array analysis, GPC-MALS; J.W. and B.Y. performed negative staining electron microscopy and analyzed data; Y.L. and J.S. performed live-cell imaging; H.S.D. performed the initial peptidisc reconstitution. B.S. performed native MS; M.S.L contributed in molecular cloning, antibody preparation, gene knockouts. S.K. trained, designed and supervised protein purification, biochemical and biophysical experiments. T.C.M. supervised electron microscopy and structure determination experiments and analysis, C.G.K and T.C. contributed to data analysis, S.K. and A.E. wrote the paper with contributions from B.Y., A.G.P. and feedback from all the authors. A.E. and S.K. conceived and supervised the project.

Acknowledgements

We thank K. C. Tsolis for preliminary SctV C-domain characterization; C. Robinson (TorA-GFP), N. Vandenberk (pBAD24-mKate2) and R. Ieva (pDR*bamE-gfp)* for constructs. This work was supported by grants (to AE and TCM): T3RecS [#G002516N; Fonds Wetenschappelijk Onderzoek (FWO); https://www.fwo.be/ and "I 2408-B22" from the Austrian Science Fund (FWF); https://www.fwf.ac.at/en/]; (to AE): DIP-BiD (#AKUL/15/40 - G0H2116N; Hercules/FWO); RUN (#RUN/16/001 KU Leuven); the FWO/F.R.S.-FNRS "Excellence of Science - EOS" programme grant #30550343) and (to AE and SK); C1 (FOscil; KU Leuven). This project was supported by funds through the Behörde für Wissenschaft, Forschung und Gleichstellung of the city of Hamburg available to TCM. B.Y. and Y.L. are Chinese Scholarship Council doctoral fellows. The funders had no role in study design, data collection and analysis, decision to publish, or preparation of the manuscript. Image data processing has been performed at the German Electron Synchrotron Centre

(DESY) using the High-Performance Computing Cluster.

Data Availability

All relevant data are within the manuscript and its Supporting Information files and are fully available without restriction.

Competing interests

The authors declare they have no competing financial interests or other conflicts of interest

References

1. Deng W, Marshall NC, Rowland JL, McCoy JM, Worrall LJ, Santos AS, et al. Assembly, structure, function and regulation of type III secretion systems. Nature reviews Microbiology. 2017.
2. Galán JE, Lara-Tejero M, Marlovits TC, Wagner SJArom. Bacterial type III secretion systems: specialized nanomachines for protein delivery into target cells. 2014;68:415-38.
3. Butan C, Lara-Tejero M, Li W, Liu J, Galán JE. High-resolution view of the type III secretion export apparatus in situ reveals membrane remodeling and a secretion pathway. 2019:709592.
4. Hu B, Lara-Tejero M, Kong Q, Galán JE, Liu J. In situ molecular architecture of the Salmonella type III secretion machine. Cell. 2017;168(6):1065-74. e10.
5. Lara-Tejero M, Galán JEJEP. The Injectisome, a Complex Nanomachine for Protein Injection into Mammalian Cells. 2019;8(2).
6. Park D, Lara-Tejero M, Waxham MN, Li W, Hu B, Galán JE, et al. Visualization of the type III secretion mediated Salmonella–host cell interface using cryo-electron tomography. 2018;7:e39514.
7. Hueck CJ. Type III protein secretion systems in bacterial pathogens of animals and plants. Microbiology and molecular biology reviews. 1998;62(2):379-433.
8. Portaliou AG, Tsolis KC, Loos MS, Zorzini V, Economou A. Type III secretion: building and operating a remarkable nanomachine. Trends in biochemical sciences. 2016;41(2):175-89.
9. Portaliou AG, Tsolis KC, Loos MS, Balabanidou V, Rayo J, Tsirigotaki A, et al. Hierarchical protein targeting and secretion is controlled by an affinity switch in the type III secretion system of enteropathogenic Escherichia coli. The EMBO journal. 2017;36(23):3517-31.
10. Abrusci P, Vergara-Irigaray M, Johnson S, Beeby MD, Hendrixson DR, Roversi P, et al. Architecture of the major component of the type III secretion system export apparatus. Nat Struct Mol Biol. 2013;20(1):99-104.
11. Terahara N, Inoue Y, Kodera N, Morimoto YV, Uchihashi T, Imada K, et al. Insight into structural remodeling of the FlhA ring responsible for bacterial flagellar type III protein export. Science advances. 2018;4(4):eaao7054.
12. Saijo-Hamano Y, Imada K, Minamino T, Kihara M, Shimada M, Kitao A, et al. Structure of the cytoplasmic domain of FlhA and implication for flagellar type III protein export. Molecular microbiology. 2010;76(1):260-8.
13. Worrall LJ, Vuckovic M, Strynadka NC. Crystal structure of the C-terminal domain of the Salmonella type III secretion system export apparatus protein InvA. Protein Science. 2010;19(5):1091-6.
14. Hara N, Morimoto YV, Kawamoto A, Namba K, Minamino TJJob. Interaction of the extreme N-terminal region of FliH with FlhA is required for efficient bacterial flagellar protein export. 2012;194(19):5353-60.
15. Ibuki T, Uchida Y, Hironaka Y, Namba K, Imada K, Minamino TJJob. Interaction between FliJ and FlhA, components of the bacterial flagellar type III export apparatus. 2013;195(3):466-73.
16. Lee P-C, Zmina SE, Stopford CM, Toska J, Rietsch AJPotNAoS. Control of type III secretion activity and substrate specificity by the cytoplasmic regulator PcrG. 2014;111(19):E2027-E36.
17. Majewski DD, Worrall LJ, Hong C, Atkinson CE, Vuckovic M, Watanabe N, et al. Cryo-EM structure of the homohexameric T3SS ATPase-central stalk complex reveals rotary ATPase-like asymmetry. 2019;10(1):626.
18. Bange G, Kümmerer N, Engel C, Bozkurt G, Wild K, Sinning I. FlhA provides the adaptor for coordinated delivery of late flagella building blocks to the type III secretion system. Proceedings of the National Academy of Sciences. 2010;107(25):11295-300.
19. Xing Q, Shi K, Portaliou A, Rossi P, Economou A, Kalodimos CG. Structures of chaperone-substrate complexes docked onto the export gate in a type III secretion system. Nature communications. 2018;9(1):1773.
20. Chen L, Ai X, Portaliou AG, Minetti CA, Remeta DP, Economou A, et al. Substrate-activated conformational switch on chaperones encodes a targeting signal in type III secretion. Cell reports. 2013;3(3):709-15.
21. Romo-Castillo M, Andrade A, Espinosa N, Monjaras Feria J, Soto E, Diaz-Guerrero M, et al. EscO, a functional and structural analog of the flagellar FliJ protein, is a positive regulator of EscN ATPase activity of the enteropathogenic Escherichia coli injectisome. Journal of bacteriology. 2014;196(12):2227-41.
22. Blaylock B, Riordan KE, Missiakas DM, Schneewind O. Characterization of the Yersinia enterocolitica type III secretion ATPase YscN and its regulator, YscL. Journal of bacteriology. 2006;188(10):3525-34.
23. Kuhlen L, Abrusci P, Johnson S, Gault J, Deme J, Caesar J, et al. Structure of the core of the type III secretion system export apparatus. Nat Struct Mol Biol. 2018;25(7):583-90.
24. Johnson S, Kuhlen L, Deme JC, Abrusci P, Lea SMJm. The Structure of an Injectisome Export Gate Demonstrates Conservation of Architecture in the Core Export Gate between Flagellar and Virulence Type III Secretion Systems. 2019;10(3):e00818-19.
25. Hu J, Worrall LJ, Vuckovic M, Hong C, Deng W, Atkinson CE, et al. T3S injectisome needle complex structures in four distinct states reveal the basis of membrane coupling and assembly. Nature microbiology. 2019.

26. Goosney DL, Gruenheid S, Finlay BBJAroc, biology d. Gut feelings: enteropathogenic E. coli (EPEC) interactions with the host. 2000;16(1):173-89.
27. Macdonald PJ, Chen Y, Mueller JD. Chromophore maturation and fluorescence fluctuation spectroscopy of fluorescent proteins in a cell-free expression system. Analytical biochemistry. 2012;421(1):291-8.
28. Barrett CM, Ray N, Thomas JD, Robinson C, Bolhuis A. Quantitative export of a reporter protein, GFP, by the twin-arginine translocation pathway in Escherichia coli. Biochemical and biophysical research communications. 2003;304(2):279-84.
29. Robinson A, McDonald JP, Caldas VE, Patel M, Wood EA, Punter CM, et al. Regulation of mutagenic DNA polymerase V activation in space and time. 2015;11(8):e1005482.
30. Radics J, Königsmaier L, Marlovits TC. Structure of a pathogenic type 3 secretion system in action. Nature Structural and Molecular Biology. 2014;21(1):82.
31. Dietsche T, Mebrhatu MT, Brunner MJ, Abrusci P, Yan J, Franz-Wachtel M, et al. Structural and functional characterization of the bacterial type III secretion export apparatus. PLoS pathogens. 2016;12(12):e1006071.
32. Wagner S, Königsmaier L, Lara-Tejero M, Lefebre M, Marlovits TC, Galán JE. Organization and coordinated assembly of the type III secretion export apparatus. Proceedings of the National Academy of Sciences. 2010;107(41):17745-50.
33. Diepold A, Wiesand U, Cornelis GR. The assembly of the export apparatus (YscR, S, T, U, V) of the Yersinia type III secretion apparatus occurs independently of other structural components and involves the formation of an YscV oligomer. Molecular microbiology. 2011;82(2):502-14.
34. Carlson ML, Young JW, Zhao Z, Fabre L, Jun D, Li J, et al. The Peptidisc, a simple method for stabilizing membrane proteins in detergent-free solution. eLife. 2018;7:e34085.
35. Gaytán MO, Monjarás Feria J, Soto E, Espinosa N, Benítez JM, Georgellis D, et al. Novel insights into the mechanism of SepL-mediated control of effector secretion in enteropathogenic Escherichia coli. MicrobiologyOpen. 2018;7(3):e00571.
36. Elliott SJ, O'Connell CB, Koutsouris A, Brinkley C, Donnenberg MS, Hecht G, et al. A gene from the locus of enterocyte effacement that is required for enteropathogenic Escherichia coli to increase tight-junction permeability encodes a chaperone for EspF. Infection and immunity. 2002;70(5):2271-7.
37. Terashima H, Kawamoto A, Tatsumi C, Namba K, Minamino T, Imada K. In vitro reconstitution of functional type III protein export and insights into flagellar assembly. MBio. 2018;9(3):e00988-18.
38. Yerushalmi G, Litvak Y, Gur-Arie L, Rosenshine I. Dynamics of expression and maturation of the type III secretion system of enteropathogenic Escherichia coli. Journal of bacteriology. 2014;196(15):2798-806.
39. Hara N, Namba K, Minamino T. Genetic characterization of conserved charged residues in the bacterial flagellar type III export protein FlhA. PloS one. 2011;6(7):e22417.
40. Kinoshita M, Hara N, Imada K, Namba K, Minamino T. Interactions of bacterial flagellar chaperone-substrate complexes with FlhA contribute to co-ordinating assembly of the flagellar filament. Molecular microbiology. 2013;90(6):1249-61.
41. Minamino T, Kinoshita M, Hara N, Takeuchi S, Hida A, Koya S, et al. Interaction of a bacterial flagellar chaperone FlgN with FlhA is required for efficient export of its cognate substrates. Molecular microbiology. 2012;83(4):775-88.
42. Yuan B, Economou A, Karamanou SJFML. Optimization of Type 3 protein secretion in enteropathogenic E. coli. 2018.
43. Long J, Shelhamer E, Darrell T, editors. Fully convolutional networks for semantic segmentation. Proceedings of the IEEE conference on computer vision and pattern recognition; 2015.
44. Martín Abadi AA, Paul Barham, Eugene Brevdo, Zhifeng Chen, Craig Citro, Greg S. Corrado, Andy Davis, Jeffrey Dean, Matthieu Devin, Sanjay Ghemawat, Ian Goodfellow, Andrew Harp, Geoffrey Irving, Michael Isard, Yangqing Jia, Rafal Jozefowicz, Lukasz Kaiser, Manjunath Kudlur, Josh Levenberg, Dan Mane, Rajat Monga, Sherry Moore, Derek Murray, Chris Olah, Mike Schuster, Jonathon Shlens, Benoit Steiner, Ilya Sutskever, Kunal Talwar, Paul Tucker, Vincent Vanhoucke, Vijay Vasudevan, Fernanda Viegas, Oriol Vinyals, Pete Warden, Martin Wattenberg, Martin Wicke, Yuan Yu, Xiaoqiang Zheng. TensorFlow: Large-Scale Machine Learning on Heterogeneous Distributed Systems. arXiv:160304467. 2016.
45. Chollet F. https://github.com/fchollet/keras. Keras. 2015.
46. Smit JH, Li Y, Warszawik EM, Herrmann A, Cordes T. ColiCoords: A Python package for the analysis of bacterial fluorescence microscopy data. PloS one. 2019;14(6):e0217524.
47. Pauli Virtanen RG, Travis E. Oliphant, Matt Haberland, Tyler Reddy, David Cournapeau, Evgeni Burovski, Pearu Peterson, Warren Weckesser, Jonathan Bright, Stéfan J. van der Walt, Matthew Brett, Joshua Wilson, K. Jarrod Millman, Nikolay Mayorov, Andrew R. J. Nelson, Eric Jones, Robert Kern, Eric Larson, CJ Carey, İlhan Polat, Yu Feng, Eric W. Moore, Jake VanderPlas, Denis Laxalde, Josef Perktold, Robert Cimrman, Ian Henriksen, E.A. Quintero, Charles R Harris, Anne M. Archibald, Antônio H. Ribeiro, Fabian Pedregosa, Paul van Mulbregt, and SciPy 1.0 Contributors. SciPy 1.0–Fundamental Algorithms for Scientific Computing in Python. arXiv:190710121. 2019.

48. Stéfan van der Walt JLS, Juan Nunez-Iglesias, François Boulogne, Joshua D. Warner, Neil Yager, Emmanuelle Gouillart, Tony Yu and the scikit-image contributors. scikit-image: Image processing in Python. Peer Journal. 2014.
49. Coelho LP. Mahotas: Open source software for scriptable computer vision. Journal of Open Research Software. 2013;1(1)(e3).
50. Wittig I, Braun H-P, Schägger HJNp. Blue native PAGE. 2006;1(1):418.
51. Stone AB. A simplified method for preparing sucrose gradients. Biochemical Journal. 1974;137(1):117.
52. Wagner T, Merino F, Stabrin M, Moriya T, Gatsogiannis C, Raunser SJb. SPHIRE-crYOLO: A fast and well-centering automated particle picker for cryo-EM. 2018:356584.
53. Zivanov J, Nakane T, Forsberg BO, Kimanius D, Hagen WJ, Lindahl E, et al. New tools for automated high-resolution cryo-EM structure determination in RELION-3. 2018;7:e42166.
54. Moriya T, Saur M, Stabrin M, Merino F, Voicu H, Huang Z, et al. High-resolution single particle analysis from electron cryo-microscopy images using SPHIRE. 2017(123):e55448.
55. Minamino T, Kinoshita M, Hara N, Takeuchi S, Hida A, Koya S, et al. Interaction of a bacterial flagellar chaperone FlgN with FlhA is required for efficient export of its cognate substrates. Molecular microbiology. 2012;83(4):775-88.
56. Kinoshita M, Hara N, Imada K, Namba K, Minamino TJMm. Interactions of bacterial flagellar chaperone–substrate complexes with FlhA contribute to co-ordinating assembly of the flagellar filament. 2013;90(6):1249-61.
57. Shen D-K, Blocker AJJPo. MxiA, MxiC and IpaD regulate substrate selection and secretion mode in the T3SS of Shigella flexneri. 2016;11(5):e0155141.
58. Yu X-J, Grabe GJ, Liu M, Mota LJ, Holden DWJm. SsaV interacts with SsaL to control the translocon-to-effector switch in the Salmonella SPI-2 type three secretion system. 2018;9(5):e01149-18.

Figure legends

Fig. 1. Subcellular localization of SctV by live cell fluorescence microscopy.

A. Cartoon representation of the EPEC injectisome. $SctV_9$ is shown in red.

B and **C.** eYFP-SctV forms distinct foci in EPEC∆*sctV* (**B**) and C41(**C**) cell peripheral. Scale bar: 5 μm. Representative images from YFP and brightfield channel are shown; *n=3* biological replicates

D-G. The distribution of control protein markers in C41 cells. The fluorescence micrographs of C41 cells expressing eYFP (**D**), TorA-GFP (**E**), BamE-GFP (**F**), and LacY-eYFP (**G**) separately. Scale bar: 5 μm. Representative images from YFP or GFP (as indicated) and brightfield channel are shown; *n=3* biological replicates

Fig. 2. Solubilization and characterization of SctV nonamers

A. Pipeline for SctV membrane complexes analysis by BN-PAGE. Following French press, lysed cells were removed and membrane fractions were harvested by ultra-centrifugation. Non-ionic detergents DDM was used to extract membrane proteins for further analysis by BN-PAGE and immuno-staining with α-SctV-C.

B. BN-PAGE analysis of EPEC-derived, DDM-solublized membrane complexes containing SctV. Membrane proteins were extracted with different concentrations of DDM, analyzed by BN-PAGE and α-SctV-C immuno-staining (lanes 1-6). ~1 MDa species containing SctV component was seen when extracted with 0.8% DDM (lane 6, bracket). A predominant ~700kDa species also appeared when extra DDM was added into 0.8% DDM sample (lane 7) migrating on the gel with the similar mass size as extractions with ~1.0% DDM (lanes 3-5). Representative images are shown; *n=3*

C. SctV complex formation in C41 cells. Complexes derived from C41 or C41/*sctV* extracted with the indicated DDM concentrations were analyzed as in B. Representative images are shown; *n=3*

D. SctRSTU complex formation in C41 cells. BN-PAGE analysis of C41 or C41/*sctRSTU*, Digitonin-solubilized membrane complexes and α-SctU-C immuno-staining. A representative image is shown; *n=3*

E-F. SctRSTU-V complex formation in C41 cells. Complexes derived from C41cells carrying compatible plasmids with *sctV* and *sctRSTU* (expressed as indicated) extracted with 0.8% DDM **(E)** or further treated with 1% DDM **(F)** and analyzed by BN-PAGE and α-SctV-C immuno-staining. Representative images are shown; *n=3*

G. C41 cells carrying compatible plasmids with *sctV* and *sctRSTU* were sequentially incubated with different inducers (as indicated) to acquire differentially gene expression. Complexes derived from those cells were extracted with 0.8% DDM, analyzed by BN-PAGE and α-SctV-C immuno-staining. Representative images are shown; *n=3*

Fig. 3. N- and C-terminal domains of SctV localization

A. Schematic representation of SctV transmembrane and cytoplasmic domains [(13); Top panel]. Sub-cellular localization of full length SctV and its sub-domains in C41 cells expressing plasmid-borne SctV, SctV-N or SctV-C (Bottom panel). Following fractionation, equal fraction volume was analyzed by 12% SDS-PAGE and immuno-staining. Tot: Total cell lysate; Cyt: cytoplasmic fraction; Mem: Membrane fraction; Sol: Solubilized membrane protein fraction. Representative images are shown; *n=3.*

B. BN-PAGE analysis of His-SctV-N in C41. The membrane fraction of C41 cells expressing plasmid-borne SctV or His-SctV-N was extracted with 1.8% DDM. Samples were analyzed by BN-PAGE and immuno-staining with an α-SctV-C or α-His antibody (lanes 1 and 2, respectively).

Fig. 4. His-SctV-C_9 purification and characterization

A. Pipeline of His-SctV-C_9 purification.

B. Purified His-SctV-C_9 was analyzed by GPC-MALS. UV traces (in black) and masses (in red) are indicated; *n=3*

C. ESI-MS analysis of native His-SctV-C_9. Spectrum of His-SctV-C_9 at different charge states (left panel) and its deconvoluted mass spectrum (right panel) are shown. *n=3*

D. Negatively stained micrographs of individual His-SctV-C_9 particles. Representative "overview" (scale bar: 20 nm), and EM 2D class sum-images (100 images/class; scale bar: 10 nm) images are shown. Cartoon representation of SctV-C_9 ring is shown with labeled distances that were obtained from $_{SE}$SctV$_9$ in electron cryotomography of the *Salmonella* injectisome (4).

Fig. 5. On-bead reconstitution of SctV$_9$ in peptidiscs

A. Pipeline of SctV higher order aggregates removal. Crude membrane fraction of C41/*his-sctV$_9$* cells, following French press disruption and ultra-centrifugation, was treated with 1.8% v/v Triton X-100 and loaded onto the 15%-35% sucrose gradient to separate His-SctV$_9$ from soluble higher order aggregates.

B. Sucrose gradient fraction containing His-SctV$_9$ were analyzed by BN-PAGE and stained with Coomassie blue. The ones without higher order aggregates were used for further peptidisc reconstitution. A representative image of such a fraction is shown; *n=3*

C. Pipeline of on-bead reconstitution into peptidiscs (His-SctV$_9$-PR) and purification. Green star = fluorescent Peptidisc peptides.

D -F. Validation of His-SctV$_9$-PR reconstitution. His-SctV$_9$-PR was analyzed by BN-PAGE followed by Coomasie blue staining (**D**) and CN-PAGE followed by silver staining (**E**) and fluorescence peptidisc detection **(F).** Representative images are shown; *n=3.*

Fig. 6. Electron microscopy analysis of His-SctV$_9$ and His-SctV-C_9

A. GPC-MALS/QELS analysis of His-SctV$_9$-PR using Superose^{TM} 6 (GE Healthcare). UV (in black), mass traces (in red) and hydrodynamic diameter (in blue) of are shown. *n=3.*

B. Negatively stained micrographs of individual His-SctV$_9$-PR particles. Representative "overview" (upper panel; scale bar: 20 nm) and "side" and "bottom views" micrographs are shown (right; scale bar: 10 nm).

C. Cartoon representation of membrane- embedded SctV$_9$ ring is shown with labeled distances that were obtained from $_{SE}$SctV$_9$ in electron cryotomography of the *Salmonella* injectisome (4).

Fig. 7. Quantitative analysis of SctV$_9$ as a functional receptor for chaperone/exported protein complexes

A. Equilibrium dissociation constants (K_d) of protein ligands for IMVs derived from EPEC and C41 cells with or without SctV (as indicated). The K_ds of CesT and CesF were also determined for IMVs that had been pre-incubated with excess of CesF or CesT, respectively (bottom); mean values (± SEM) are shown; *n=6.*

B. Structure model of $_{EPEC}$SctV-C protomer (9) shown as ribbon. Chaperone binding domains are shown in different colors as indicated.

C. Chaperone binding domains on SctV C$_9$ model structure. Surface model of $_{EPEC}$CSctV-C$_9$ (9), derived from the proposed $_{SF}$SctV-C$_9$ model [(10); side (top) and bottom view]. Experimentally-determined chaperone binding sites from previous studies (9, 18, 19, 39, 55-58) are coloured red in one protomer (dark grey) and ones from this study coloured yellow in two adjacent protomers of the model (light grey).

D. EspA secretion and HeLa cell infection from EPEC∆*sctV* /*sctV* wt or derivatives were performed and quantified as previously (9). WT secretion or infection was considered 100%; all other values are expressed as % of this. *n=3* biological replicates. Unpaired parametric t-test, 95% confidence interval was performed; (*): p-values <0,001.

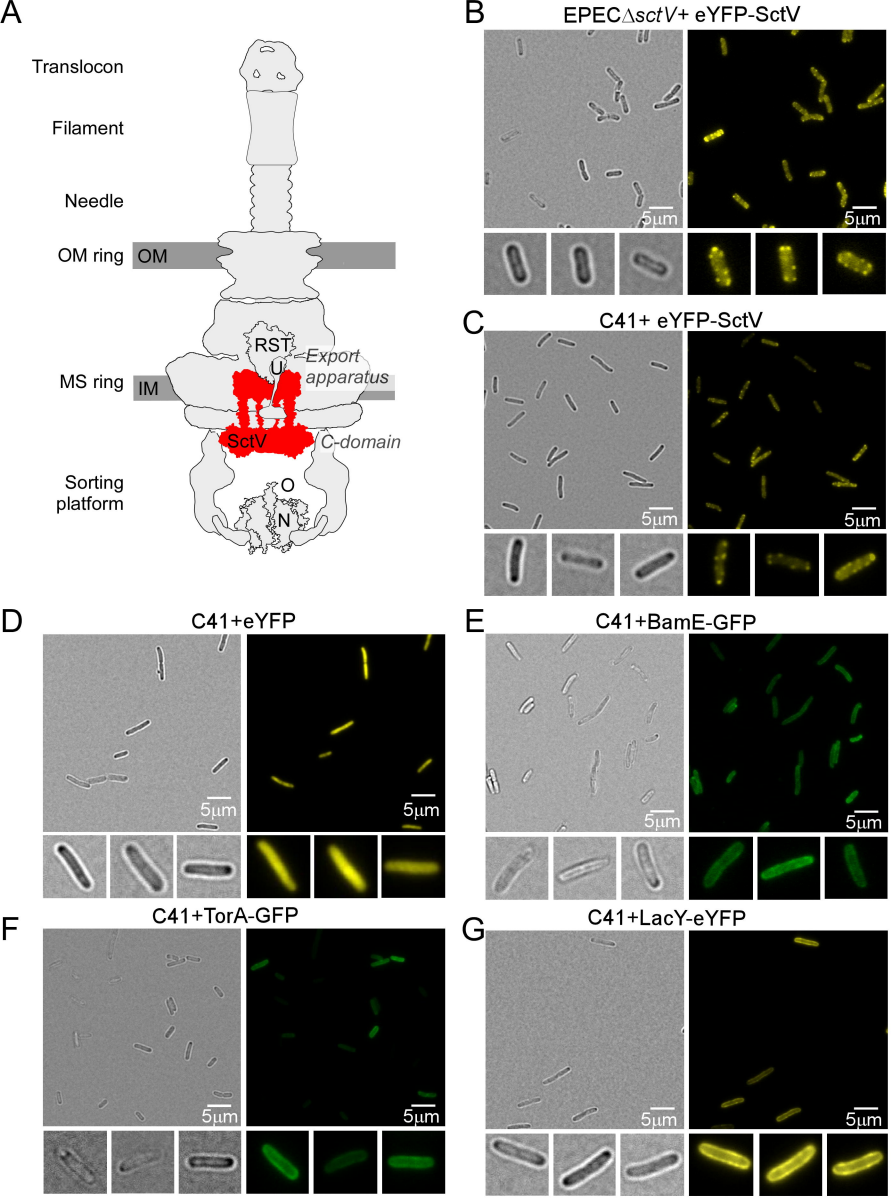

Fig.1 Yuan et al,

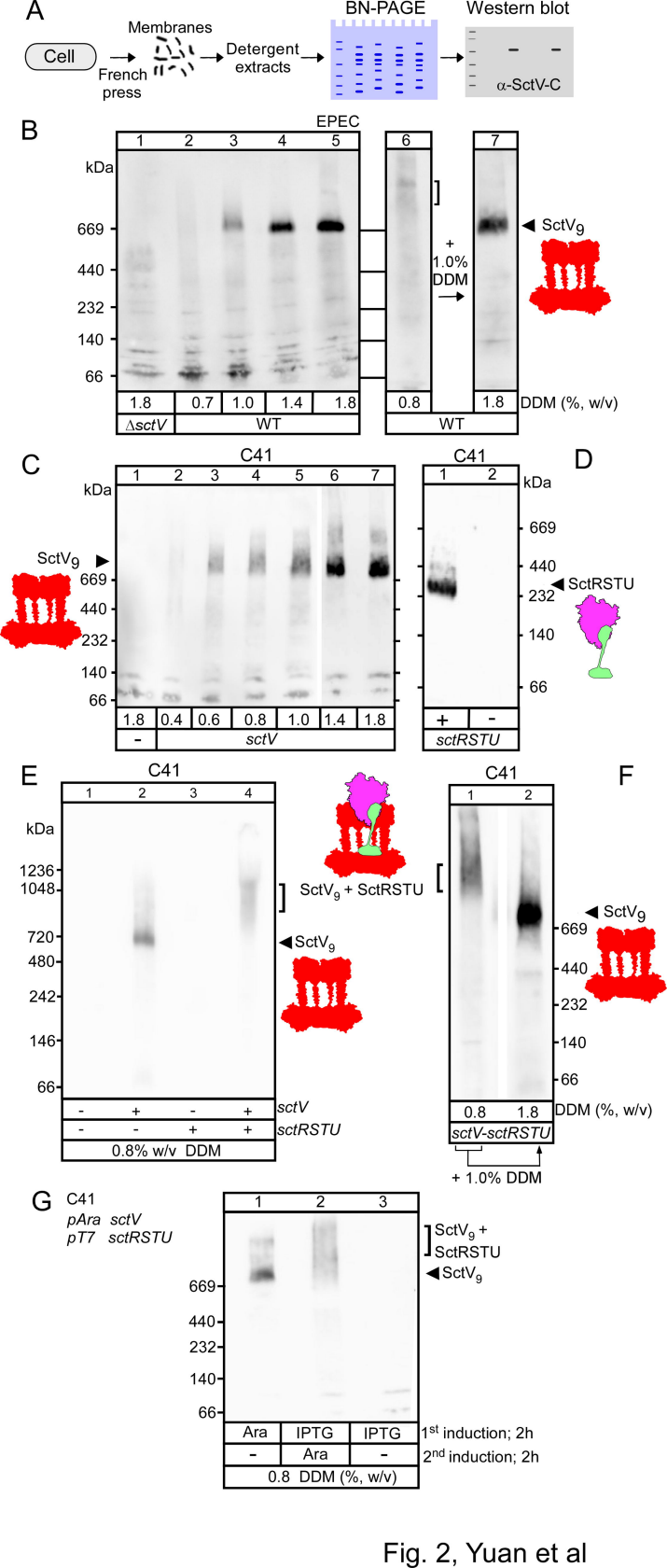

Fig. 2, Yuan et al

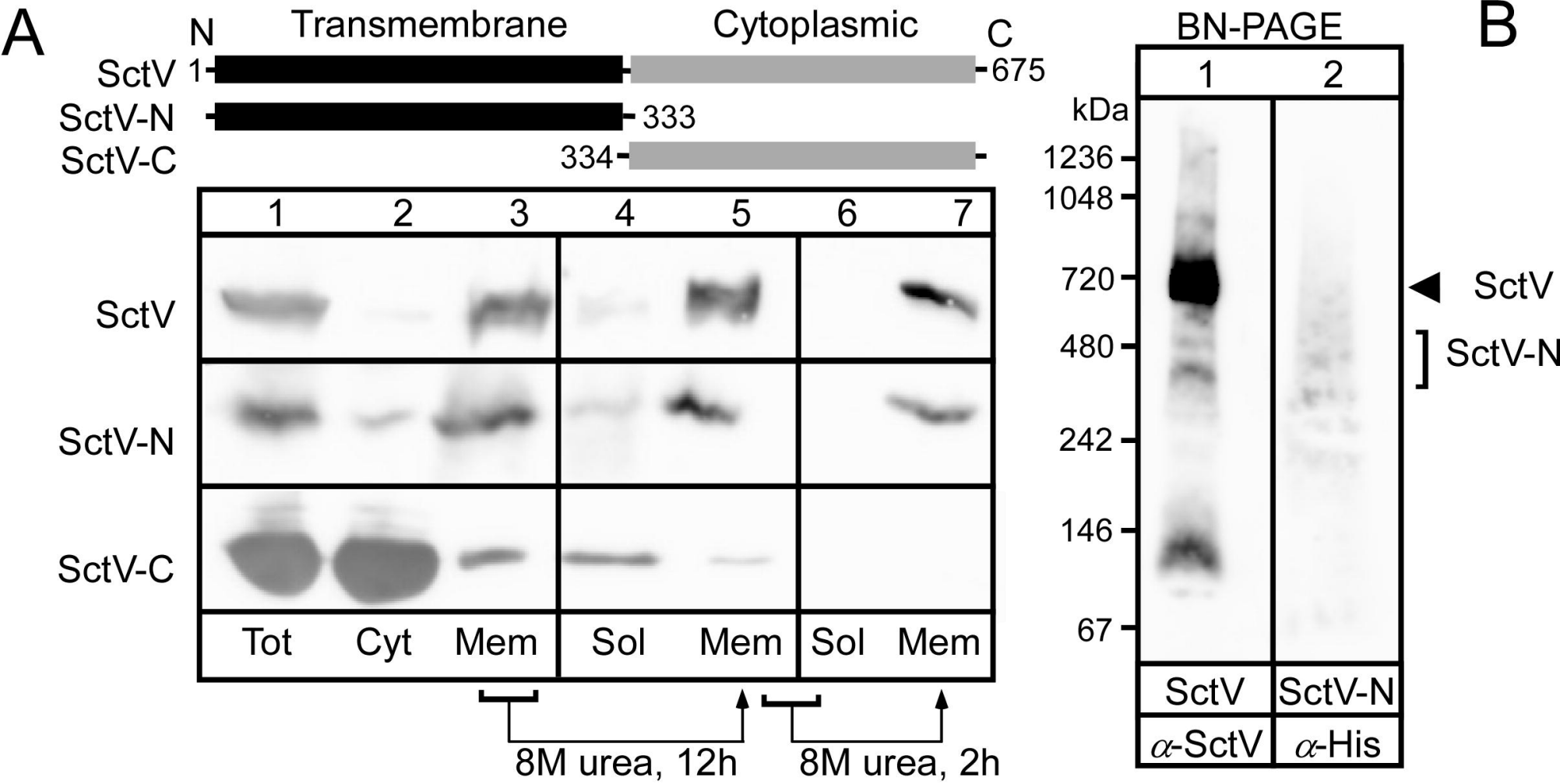

Fig. 3, Yuan et al

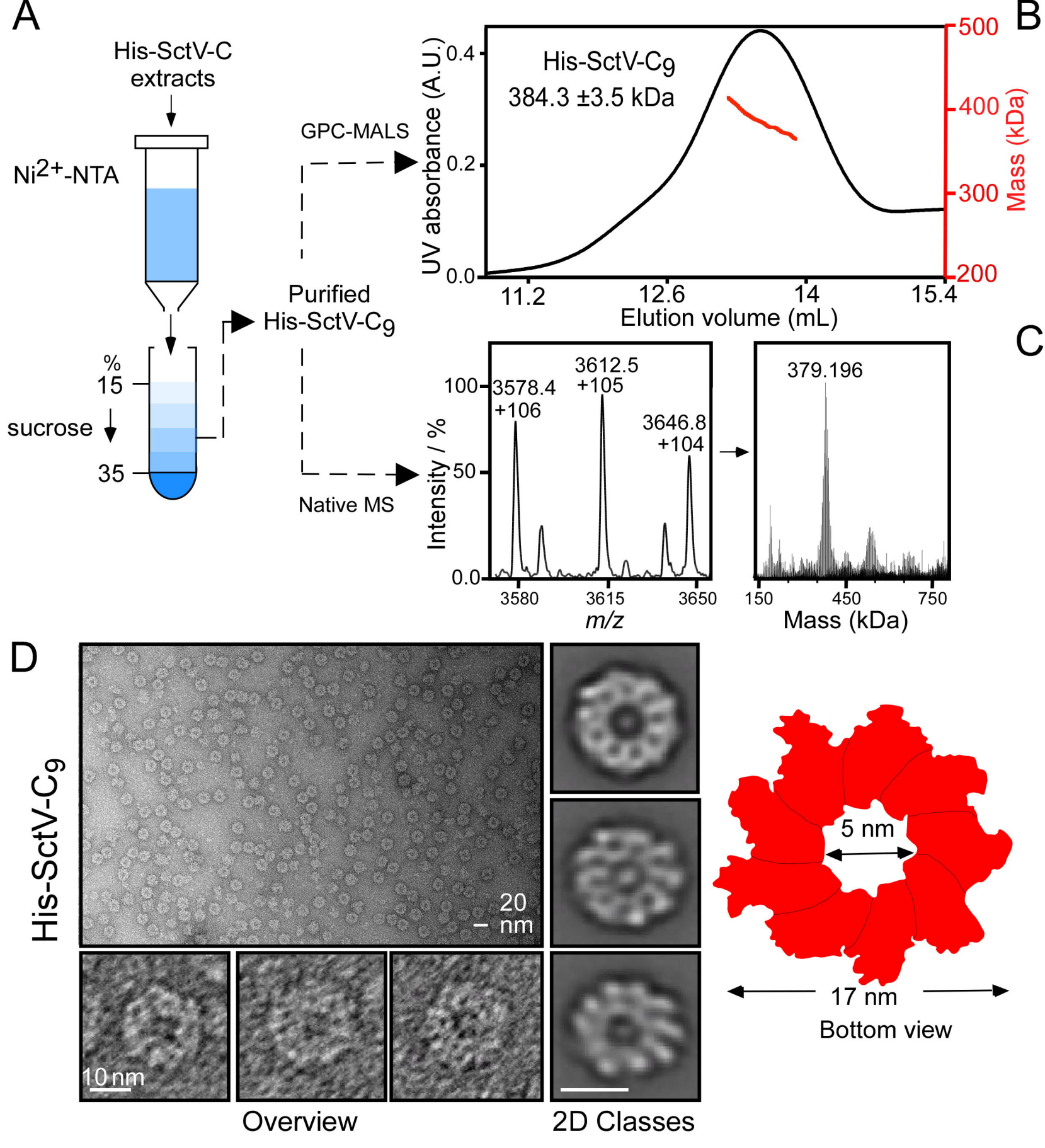

Fig. 4, Yuan et al

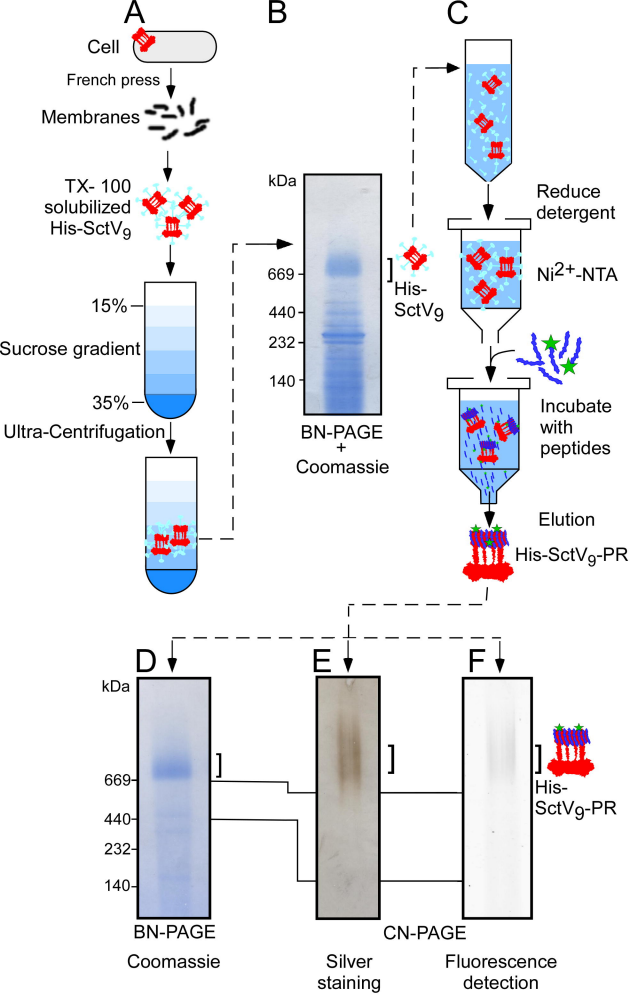

Fig. 5, Yuan et al

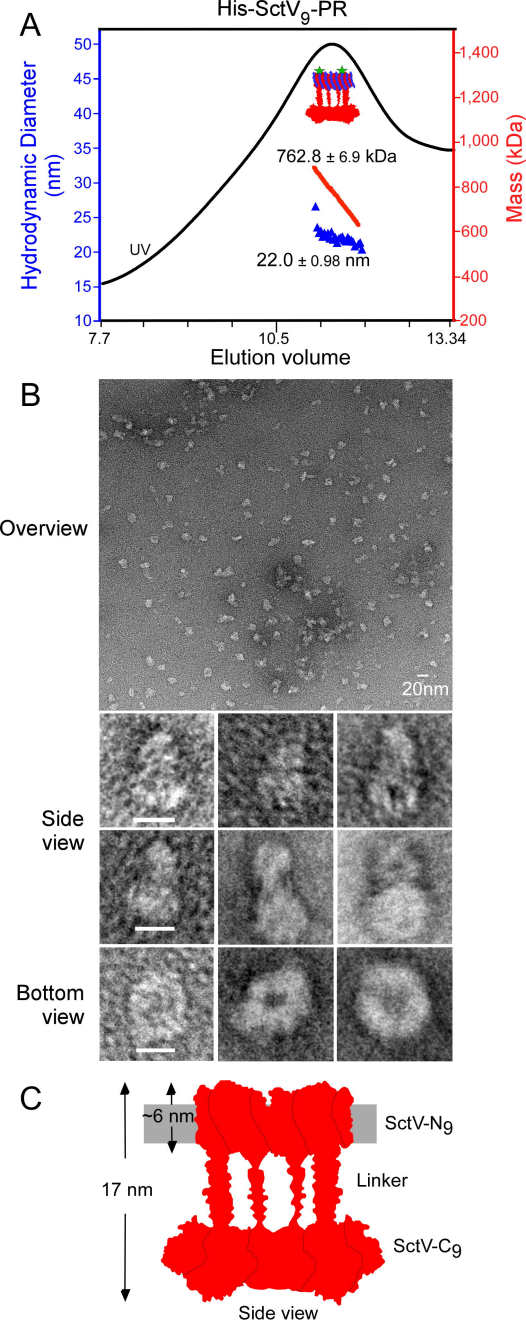

Fig. 6, Yuan et al

A

Affinity (K_d, μM)

IMVs	C41		EPECΔ*sctV*			
sctV	-	wt	-	wt	mutated γ	mutated ε
protein ligand: CesT/Tir	NM	0.54(±0.08)	NM	0.38(±0.08)	2.11 (±0.76)	1.27(±0.31)
CesF/EspF	NM	0.51(±0.09)	NM	0.42(±0.08)	1.51 (±0.49)	NT
CesT	NM	0.50(±0.17)				
CesF	NM	0.60(±0.20)				
CesT(+6μM CesF)		NM				
CesF(+6μM CesT)		NM				

B

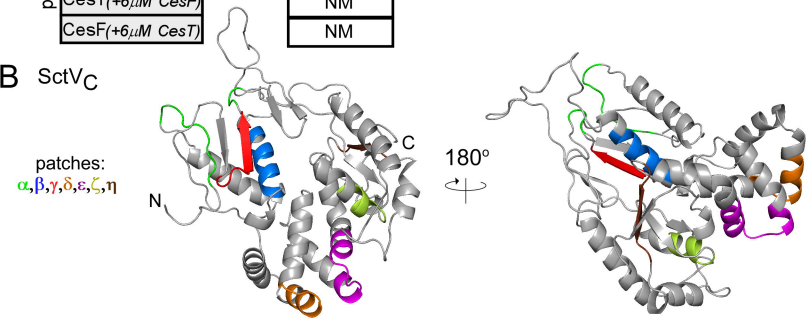

C

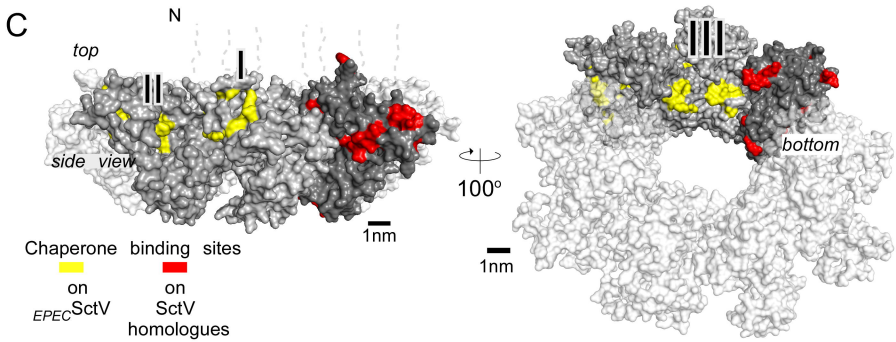

D

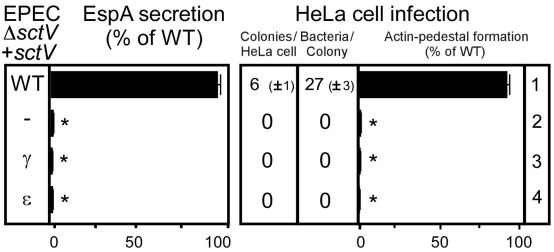

Fig. 7, Yuan et al